Contents lists available at ScienceDirect

Nuclear Inst. and Methods in Physics Research, B

BEAM INTERACTIONS WITH MATERIALS AND ATOMS

Beam optimization of a heavy ion microbeam for targeted irradiation of mitochondria in human cells

Sarah Rudigkeit [*], Nicole Matejka, Matthias Sammer, Dietrich W.M. Walsh, Günther Dollinger, Judith Reindl

Institut für angewandte Physik und Messtechnik (LRT2), Universität der Bundeswehr München, Werner-Heisenberg-Weg 39, 85577 Neubiberg, Germany

ABSTRACT

Mitochondria, organelles of the cytoplasm, are the power plants of the cell and thus their function is important for the survival of cells. Mitochondria are known to depolarize after targeted irradiation, but the effects on cells are still unclear. The aim of this work is to investigate the effects of mitochondrial depolarization on growth and survival of cells. We performed targeted irradiation with 55 MeV C^{5+}-ions at the ion-microbeam SNAKE at the 14 MV tandem accelerator in Garching near Munich, with a beam spot size of ~1 μm. Approx. 6% of the mitochondrial area was irradiated in 74 cells with 5,120 carbon ions homogenously distributed over a square area of 13.2 μm^2. Cell growth was investigated by observing the cells for 3.5 days via live-cell phase-contrast microscopy and evaluating the number of vital cells. While the number of irradiated cells remained constant during the observation, the unirradiated control group showed exponential growth. An additional particle track detector test with polycarbonate revealed that 4% parasitic ions hit the cells up to 500 μm away from the target, forming a so-called halo and inducing a mean parasitic dose of (2 ± 2) Gy on the cells. This dose alone, when applied in cell nuclei, is large enough to reduce the survival and growth of cells significantly and overrides any effects caused by targeted irradiation of mitochondria. Subsequently, several methods to reduce the halo were investigated. A significant reduction in halo size and number of ions in the halo could be achieved by using C^{6+}-ions instead of C^{5+}-ions. The slit openings, correction of lens errors, and the beam spot size had minor influence on the halo size but could achieve a reduction in halo dose. Overall, a 97% reduction in halo area and a halving of halo dose were achieved.

1. Introduction

Since the 1950s, the main dogma in radiobiology has been that the cell nucleus, which contains DNA, is the main target of radiation. In this context, irradiation using microbeams was very successful in studying radiation effects on sub-cellular structures. Microbeams were developed for focusing charged ions or x-rays to beam spot sizes of a few micrometers or even smaller. With such facilities, cells can be targeted for irradiation with high accuracy in subcellular compartments and whereby a counted number of ions can be delivered. Therefore, it can be investigated how different organelles react to irradiation [1–3]. Using this technique, researchers could show that the cytoplasm is radioresistant while the nucleus is very radiosensitive [4–6], supporting the overall accepted paradigm. Also, other effects like the bystander effects [7–10] or the track structures and the foci induction along ionization paths [2,11–13] are investigated by the use of microbeams. In contrast,

in several studies, cellular radiation effects could be found when irradiating the cell cytoplasm. The effects were mainly visible in the inhibition of DNA synthesis and oxidative stress-related reactions [14–17]. These experiments add a level of complexity to the radiation effects on cells. There seem to be effects beyond the pure DNA damage, which cause radiation response in cells.

One prominent target in the cytoplasm, which is connected to cellular radiation response, are mitochondria [18]. Mitochondria, are the power plants of the cell, converting ADP (adenosine diphosphate) to ATP (adenosine triphosphate), thus producing the primary energy source for the cell. Therefore, they are essential for cell survival. Tumor cells in particular are highly dependent on the functionality of their mitochondria due to their increased metabolism [19]. In 2017, D.W.M. Walsh and coworkers could show that the targeted irradiation of mitochondria leads to the depolarization of the mitochondrial membrane [1]. This depolarization results in the release of cytochrome *c*. If

---

cytochrome *c* is present in large quantities in the cell, apoptosis can be induced [20]. Walsh et al. only investigated short-term radiation effects on mitochondria.

Therefore, the goal of this consecutive study is to investigate the long-term reactions of human tumor cells after depolarizing mitochondria with targeted irradiation. Small mitochondrial areas in single cells were irradiated using 55 MeV 5-times positively charged carbon ions at the microbeam SNAKE at Meier-Leibniz-Laboratorium in Munich. After irradiation, the cells were imaged for 3.5 days via phase contrast microscopy and cell growth was evaluated on the resulting videos. Furthermore, principle investigations were made on beam spot size, the number of ions outside the target, and the used charge state of the ions. Especially the ions, which hit the sample outside of the focal spot, are important for high-LET targeted irradiation, as a single ion hit in the cell nucleus can already cause cell death [21,22]. All beam properties were measured using etched polycarbonate nuclear track detectors as it is common in the microbeam community [23–25].

The polycarbonate measurement of the irradiated target shows a halo of 4% of the irradiated ions, which hit the polycarbonate foil up to 500 μm away from the target. As this halo is big enough to damage cell nuclei on the sample, an optimization of the microbeam was necessary. In this study, we present the optimization process. As a first step, we change the ion sort from C^{5+} ions to C^{6+} ions. Additionally, we had to adjust the slit openings to yield a higher ion throughput and to correct lens errors by slightly changing the magnetic fields of the superconducting lenses of SNAKE by energizing correction wires at the pole pieces. With these optimizations, the halo could be reduced to 0.76% ions in the halo of all irradiated ions with a maximum distance of 167 μm.

2. Methods

2.1. Microbeam facility SNAKE

The experiments were performed at the Maier-Leibnitz-Laboratory in Garching near Munich at the microbeam facility SNAKE (**S**uperconducting **N**anoprobe for **A**pplied nuclear (**K**ernphysikalische-) **E**xperiments). One-time negatively charged carbon ions were accelerated in a linear accelerator of the type Tandem-van de Graaff. In the center of the accelerator, the ions traversed a thin carbon stripper foil, that removes electrons from the ions. The stripped ions were accelerated a second time with the terminal voltage. After leaving the accelerator, the ions passed a 90°-magnet, where they were sorted due to their energy and charge. In this study, 55 MeV C^{5+} and C^{6+} ions were used. At the focal point of the 90°-magnet, the beam was cut with two pairs of slits, so-called object slits. Thereby, one pair cuts the beam in horizontal direction perpendicular to the beam, in the following defined as x-direction, and the other pair cuts the beam in vertical direction perpendicular to the beam, defined as y-direction. These slits define the beam spot size of the object, which is focused via superconducting lenses to the target. Additionally, the divergence of the beam was reduced with another two pairs of slits down to 10 μrad. The slit system is described in more detail in [26,27]. All slits consist of mechanically lapped tungsten at a cylindrical geometry with a top radius of r = 100 mm, which provide a small transparency zone for beam particles. Downstream these slit systems, the beam was further focused to a beam spot size of approx. 1 μm using three superconducting magnetic quadrupoles, as described in [27] in detail. The first two quadrupoles were used for focusing in x-direction, whereas the last lens was used for y-focusing. Spherical aberrations in this lens system can be corrected by energizing superconducting wires, so-called supraloops. The supraloops eliminate asymmetries in the magnetic field, which occur due to mechanical imperfections in the lens system. These imperfections lead to asymmetric magnetic fields if the net magnetic flux within all four poles of one quadrupole is not the same, dominated by induced sextupole fields. The supraloops correct for the field asymmetries, as they are connecting neighboring pole shoes, and

can be actively regulated by applying a current from the outside. A more detailed description of the correction wires can be found in [28].

2.2. Ion focusing

Prior to focusing the object and divergence, apertures were centered on the transmitted beam. This was done in a two-stage process. First, the maximum current measured with a cup placed behind the focusing unit in vacuum was cut out in both x and y direction. This was possible as for each aperture both jaws can be moved independently. In this step, the object which was used for focusing was defined as a 200 μm × 200 μm sized square. In the second step, a mesh was inserted in the beam path, to allow an optical visualization of the beam on a YAG scintillator placed on the microscope at the beam exit. This mesh induced a grid-like point pattern having 15 columns and lines. Here, the exact middle of the beam was defined by applying low currents on the focusing lenses to be able to see the outer regions of the beam and taking the 5 columns and lines of points in the middle. These 25 points were focused by eye to the smallest possible size using a 20× objective first and a 40× objective for fine focus. After this, the mesh was moved out of the beam and the beam was corrected for the rotational misalignment of the lenses by an additional small quadrupole rotated 45° to the orientation of the three main quadrupoles of SNAKE, allowing for the smallest possible focus. From September 2018, the head of the lens supporting structure was shielded from noise originating from vacuum pumps and experimental equipment in the experimental hall by a housing of egg foam with a knob height of 4 cm. The outside noise caused mechanical vibration in the lens system, which needed to be suppressed to achieve the best beam spot size. Finally, the beam was corrected for blurring by electromagnetic fields originating from all devices connected to electrical power supply. This distortion was in phase with the 50 Hz of the power supply system and could therefore be actively corrected using the x and y deflection plates. First, the 50 Hz synchronized amplitude of deflection by the parasitic fields was determined in x and y direction and then the inverted signal was applied to the beam. A detailed description can be found in [29].

2.3. Single ion irradiation

For single ion irradiation, a scintillator (BC400, Fa. Bicron (Saint-Gobain Crystals), France) is placed behind the irradiated sample and is coupled to a photomultiplier tube (PMT, Metal Package, R7400P, Fa. Hamamatsu, Germany), which can detect single transmitted ions. The PMT-based detection is connected to the hardware electronics and the software. The hardware counts the ions and sends a trigger signal if a prescribed number of ions has been detected. The trigger is used by the software to set the next point of an irradiation pattern. To ensure that after reaching the defined number of ions per irradiated spot the irradiation stops, an ultrafast electrostatic beam switch is also controlled by hard- and software. The beam switch is an electrostatic chopper that deflects the beam approx. 10 m in front of the focusing unit by applying 3 kV voltage on condensator plates perpendicular to the beam. This chopper can switch off the beam within 1 μs including a transfer time for ions for the target that have already passed the chopper before it was closed. The irradiation is started by giving an initial trigger signal to the chopper to open it. Then irradiation is performed at a single spot until the desired number of ions is reached, then a signal is given to the chopper to close and the deflection plates take the new voltage to deflect the beam to the next position. After this, a trigger is given to reset the counter and open the chopper and irradiation starts again. This is done until all defined positions or targets are irradiated.

The ion detection system can be run in two modes: for live-cell irradiation and for beam measurements using polycarbonate foil. For beam measurements, a scintillator is directly coupled to a photomultiplier tube and placed in the objective revolver of the microscope behind the sample. This system is easy to use and very robust ensuring a

high signal-to-noise ratio. For live-cell imaging, this system can't be used as an objective needs to be put behind the sample to be able to do imaging directly before and after irradiation. Therefore, another detection system was developed, where an EJ 228 scintillator (Eljen Technology, US) serves as growth substrate of the cells. The scintillation light is guided through the microscope beam path to a camera port where the PMT is mounted. This system allows for a fast switch between imaging and irradiation to ensure the best imaging quality, as the optical components are not moved [30].

2.4. Measurement of the beam spot size

For the measurement of the beam spot size, a matrix with one ion per point and a point distance of 10 µm or 12 µm was irradiated on a polycarbonate foil. After irradiation, the polycarbonate was etched with 6.3 M NaOH-acid for 45 min at 70 °C. The etched foil was then cleaned with ethanol and fixed between an object glass and a cover glass with water droplets. Then, the ion tracks were imaged with a 40x objective (Plan-Apochromat 40×/0,95 Korr Ph3 M27, Zeiss, Germany) with brightfield transmission light illumination at an inverted microscope (Axio Observer Z1, Zeiss, Germany) and a field of view of 225 µm × 168 µm. In each image, the center of mass of each ion hit was determined using FIJI software [31]. First, the images were inverted and background corrected with a rolling ball algorithm with 10 pixels size, using the preinstalled plugins. Then, the contrast was enhanced and the image was rotated such that the matrix lines were oriented horizontally. A 3D object counter was applied, which determined the center of masses and collected it in a table. In the next step, a theoretical matrix was adapted to the actual measurement by taking rotation, translation, distortion, and strain into account. For each matrix point, the deviation from the best-fitted theoretical matrix is determined and a Gaussian function is fitted to the histogram of hits with a bin size of 0.1 µm in x and y direction. The full width at half maximum of the Gaussian functions corresponds to the x and y beam size. This method is in detail described in [29].

2.5. Halo measurements with polycarbonate

Polycarbonate foils of several cm in size were irradiated with a large number of ions in two geometries. The first geometry is a 8×8 matrix with a point distance of 0.52 µm, resulting in a target size of 13.2 µm^2, with 80 ions per point and thus 5,120 ions in total. A homogeneous dose distribution within the matrix can be assumed due to the beam spot size of approx.1 µm. For the second geometry, 10,000 ions were irradiated in a single point. The foils were etched and imaged as described in section 2.4, resulting in 1.6 µm sized circular damages. To ensure that all hits are on the resulting image, a 5×5 image matrix with 20% overlap and a total size of 940 µm × 704 µm was recorded. For targets with a larger halo, a 9×9 image matrix with a size of 1656 µm × 1241 µm was recorded. Five focus levels with a distance of 1 µm were recorded to counteract thickness differences in the polycarbonate. Images were

stitched with the stitching tool in ImageJ software [32]. The target area, where the visible ion hits overlap and counting is impossible was labeled with a polygon shape. All other hits were labeled manually with the multipoint selection tool of Fiji software [31].

2.6. Cell seeding and staining

HeLa cells were grown in RPMI (RPMI 1640, Sigma Aldrich) completed with 10% v/v FCS (Sigma Aldrich) and 100 mg/ml penicillin–streptomycin (Sigma Aldrich) at 37 °C, 95% humidity, and 5% CO$_2$ saturated atmosphere.

Cells were seeded in specially designed live-cell imaging containers, which use the EJ 228 scintillator as a growth substrate, 24 h prior to irradiation (Fig. 1). These containers allow to irradiate and consecutively image cells, while they are covered with medium and temperature is maintained at 37 °C. For this purpose, the containers can be sealed with a cover plate, which has a 4.7 µm thick polypropylene beam entrance window. The temperature is maintained as the stage, container, and beam exit nozzle are heated to 37 °C during irradiation and imaging. A detailed description of the live-cell imaging containers can be found in Hable et al. [30].

The scintillator was coated with CellTak (Corning, 3.5 µg/cm^2), which was dissolved in NaHCO$_3$ (Sigma, 30x buffer, 0.1 M) a day before cell seeding, to increase cell attachment and growth. After 20 min of incubation at room temperature, the Celltak was removed and the sample was washed with water. The samples had to dry at air for 24 h and were sterilized with UV light for half an hour.

Cells were seeded in 4well (Microinsert 4well Fultrac, Ibidi), silicone inserts, which are self-attaching and were placed in the middle of the scintillator window, as shown in Fig. 1. The inserts contain four cones with openings towards the bottom with a diameter of 0.4 mm. This allows for plating of 4 cell isles containing approx. 50 cells at defined positions on the scintillator. Low cell numbers are necessary to be able to irradiate all cells in a reasonable time. For plating, the cones of the insert were filled with 10 µl of cell solution containing 70.000 cells/ml and the sample was incubated for 1 h at 37 °C. In this time, 30 – 50 cells adhere to the scintillator in the growth areas of the insert. When cells are attached to the scintillator, the insert was removed and the sample was incubated for another 23 h. With this technique, the seeding of four well-defined cell areas with a distance of 1 cm to each other on one sample was achieved.

30 min before irradiation, mitochondria of all cells (cells for irradiation and sham cells) were stained with TMRE (Tetramethylrhodamine-Ethylester, ThermoFisher). For this procedure, the medium was removed and 50 nM TMRE in medium was added to the cells. After 25 min of incubation at 37 °C, the solution was removed and the cells were washed once with medium. Finally, the LCI container was filled with 6 ml medium and the container was closed and mounted at the 90°-tilted microscope (Axiovert200M, Zeiss) located at the SNAKE beam line. Here, the sample was heated to 37 °C.
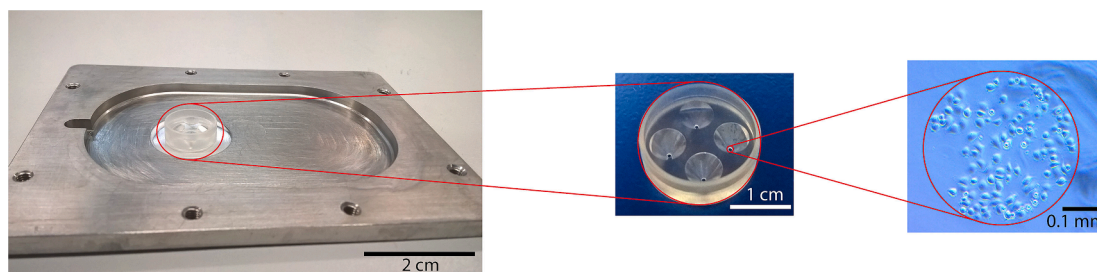

Fig. 1. The special cell seeding method for seeding low numbers of cells. The insert was placed on the scintillator window of the LCI, depicted on the left. In the middle, the insert is shown, which has four cones with openings towards the bottom and on the right, the growth area is shown. The diameter of the growth area is 0.4 mm.

2.7. Cell irradiation and imaging

Cells were irradiated with 55 MeV C^{5+} ions. Energy loss in the 7.5 μm kapton beam exit window of the beam tube, the 4.7 μm polypropylene beam entrance window of the sample and the approximately 20 μm thick medium layer covering the cells lead to an ion energy of 43 MeV and an LET in water of 365 keV/μm at the cell level.

For irradiation, the cells were imaged using a 40x objective (Plan-Apochromat 40×/0.95 Korr Ph3 M27, Zeiss, Germany), the 555 nm LED, and an appropriate filter cube (43HE Zeiss) to detect the fluorescent light of TMRE. With this setup, the mitochondria in every cell could be visualized and therefore the location of the targets could be determined for the irradiation. In each cell, a spot in the mitochondrial area located in the cytoplasm was manually defined as irradiation spot, as depicted in Fig. 2A. If the mitochondrial area was too small for the target, the target was located into the nucleus to ensure cell death of this cell and to avoid any contribution of these cells to cell growth. For the experiments of this manuscript, one cell area was irradiated and a second one was unirradiated and kept as a sham control. In the first, the cells were irradiated with square-shaped targets. A target consists of a 8 × 8 matrix with matrix point distances of 0.52 μm resulting in a homogenous dose distribution on a field of 13.2 μm^2. Every matrix point was irradiated with 80 carbon ions, therefore in the whole target area, 5,120 ions were deposited. The locations of the targets in the cell area were chosen manually. Manual target definition and irradiation took 1 h.

After irradiation, the sample was moved to an inverted microscope (Axio Observer Z1, Zeiss) with a motorized stage. Every 15 min, the cells of each area were recorded with a 20x objective (LD A-Plan 20x/0.30 Ph1, Zeiss, Germany) in phase-contrast illumination mode using condenser annulus pH 2. For video recording, the cell isles were imaged on three (unirradiated cell isle) or four spots (8 × 8 irradiated cell isle). This approach ensures that all cells are recorded on the videos, even if the cell colony grows and the cells, therefore, are distributed over more space. During the whole observation, the cells were incubated at 37 °C and 5% CO_2 with a stage-top incubator (Stage Top Incubator, Tokai Hit).

3. Results and discussion

3.1. Cell survival after targeted irradiation of mitochondria

The first aim of this study was to investigate the effects on cell growth after depolarizing approx. 6% of mitochondria in a cell. Cells were seeded in small, well-defined circular areas 24 h before irradiation using a newly established cell seeding method. With this method, a low number of 30–50 cells was seeded in each cell area as depicted in Fig. 1.

This number is small enough to perform targeted irradiation on all cells in less than 1 h. The mitochondria stained with fluorescent TMRE were imaged with the microscope at the beam line. The targeted irradiation was performed by manually choosing the locations of the targets in the images taken directly before irradiation. Thereby, every target was located in the mitochondrial area of each cell, as shown in Fig. 2A. To avoid movement of the cells and therefore bad targeting, the time between pre-irradiation image and irradiation did not exceed 5 min. Each cell was irradiated with 5,120 55 MeV carbon ions with an LET of 365 keV/μm in a 13.2 μm^2 area, corresponding to a dose of 22.7 kGy in the target area. Such a high dose, which was deposited in the target area, was necessary to depolarize mitochondria to switch them off, as shown in a previous study [1].

After irradiation cells were imaged for 3.5 days at a live-cell imaging microscope. Each position was imaged every 15 min using phase contrast imaging. The unirradiated cell isle was recorded on three positions and the irradiated cell isle on four positions to ensure that all cells are recorded even if the cell colony grows and the cells are therefore distributed over more space. The videos are evaluated by counting the vital cells on each frame based on the following equation:

$$N(t) = N(t-1) - N_{cell\ death}(t) + N_{cell\ division}(t)$$

where $N(t)$ is the number of vital cells at frame t, $N_{cell\ death}(t)$ is the number of cell deaths and $N_{cell\ division}(t)$ is the number of cell divisions, which occurred in frame t. The cell growth rate is calculated as the normalized number of vital cells per frame: $n(t) = \frac{N(t)}{N(0)}$ as shown in Fig. 2B, where $N(0)$ is the number of vital cells in the first frame. The error bars depict the standard deviation between the three or four videos recorded of the cell isles. The number of vital cells in the unirradiated group increased exponentially. After 3.5 days, the population of unirradiated cells increased almost sixfold, whereas the cell number of the irradiated group remains constant.

As described, we have evaluated the cell growth after targeted irradiation of mitochondria of human HeLa cells. Since 1953, the overall consensus in radiobiology is that the cytoplasm is less radio-sensitive than the nucleus. H.T. Epstein published a comprehensive communication, where he argued that the nucleic acid volume, i.e. the DNA is the sensitive target for radiation [33]. This came along with the development of the first biological microbeam of R.E. Zirkle and W. Bloom in the same year [4]. They irradiated 2.5 μm sized areas in mitotic cells using 2 MeV protons. Radiation-induced effects were only visible in the DNA around the ion traversal and not after cytoplasmic irradiation. Since then, several studies showed that cytoplasmic irradiation has no or less cytotoxic effects using either UV microbeams, ion microbeams, or short-ranged ion irradiation. For example, T.R. Munro irradiated cells from the side with alpha particles from a polonium-tipped microneedle [6].
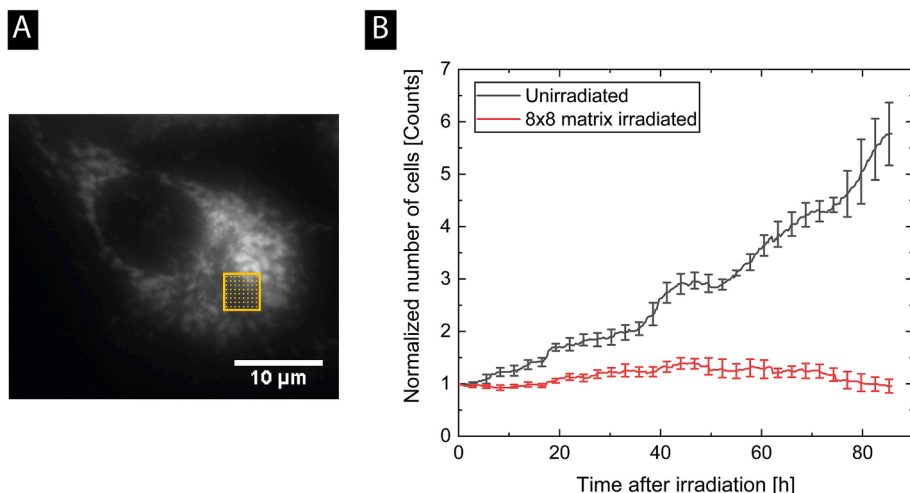

Fig. 2. Targeted irradiation of mitochondria and cell growth assessment. In A, the target area is indicated with a yellow box with which the mitochondrial area of each cell was irradiated. Whereas in B, the cell growth is shown. In this graph, the number of vital cells was normalized to the number of vital cells on the first frame. The cells were irradiated with a 8 × 8 matrix with an area of 13.2 μm^2 in the mitochondrial area. While the number of vital cells increased exponentially for the unirradiated group, the number of vital cells in the irradiated group stayed constant for the whole observation time of 3.5 days. This experiment was performed once, due to the extent of the measured halo discussed in Sections 3.2 and 3.3. (For interpretation of the references to colour in this figure legend, the reader is referred to the web version of this article.)

The distance of the needle to the cell nucleus was chosen, such that the alpha particles didn't reach the cell nucleus. No effect on the survival of cells was measured with irradiation of >250 Gy alpha particles to the cytoplasm. These results could be confirmed by many other studies as summarized in [34], leading to the paradigm of non-radiosensitive cytoplasm. However, in the last 70 years, there were also studies pointing to some radiation effects in the cytoplasm. Especially hindering effects on DNA synthesis were reported [14–17]. These and other so-called bystander effects of cytoplasmic irradiation were mainly traced back to the induction of cytotoxins, which then damaged the DNA [18,34]. Overall, the dose needed to induce measurable effects by irradiation of cytoplasmic regions is much, up to several hundred times, higher compared to the dose needed with nuclear irradiation. Furthermore, the effects were much smaller compared to nuclear irradiation. These findings challenge the overall accepted dogma of the cell nucleus being the main target of radiation. One cell organelle, which might play a role in the cellular response to radiation are mitochondria [1,18], as mitochondria are the power plants of the cells and the only other location in the cell besides the cell nucleus, where DNA is present. Mitochondria seem to play a major role in radiation-induced oxidative stress and therefore can be a key player in the cellular radiation response network [18,35]. Furthermore, Walsh and co-workers were able to depolarize mitochondria with high local doses of 55 MeV carbon ion and 3 MeV proton irradiation using microbeams SNAKE and AIFIRA [1]. They investigated mitochondrial depolarization using TMRE as an indicator of an intact mitochondrial membrane potential and demonstrated by fluorescence measurements that the loss of TMRE signal after irradiation was due to loss of mitochondrial membrane potential and not to ion-induced bleaching. In the current study, we showed that depolarizing, and therefore inactivating, approx. 6% of mitochondria by irradiating >5000 ions in the mitochondrial area leads to a total growth stop of the cells. The underlying mechanisms for the depolarization are still unclear and further investigations are necessary. Structural changes due to direct interaction or radiation-induced reactive oxygen species are thinkable. The extraordinarily high amount of produced ROS when irradiating such high doses (approx. 22.7 kGy in the target area) can also induce intracellular bystander effects by causing for example mutations in the DNA. Additionally, such an amount of ROS can lead to significant oxidative stress that might lead to growth arrest [36,37]. Furthermore, it is possible that other organelles in the cytoplasm were hit when targeting mitochondria, which could further affect cell growth. However, previous studies showed that the traversal of many high-LET particles (up to 250 alpha particles) in the cytoplasm has minor effects on the overall cell survival [6,38] compared to the traversal of few high-LET particles in the nucleus [39]. In this study, >5000 ions (approx. 22.7 kGy in the target area) were irradiated in the cytoplasm which is a much higher dose than usually applied. The effects of such a high dose in the cytoplasm on cell survival are unknown, as they were never tested before to our knowledge. The total growth stop of cells observed in this study is not entirely unexpected, but this extent of growth stop seems unusual. Therefore, the results of the presented study were questioned. Experiments of high-LET particle irradiation of non-nuclear areas always pose the risk of parasitic nuclear hits, which result in high cell killing. In general, a single carbon ion induces a mean dose of 0.73 Gy to a cell nucleus. Considering cell survival curves measured by Bedford and Hall and Friedrich et al., a relative biological effectiveness of the carbon ions used in this experiment of 4 and a cell survival below 50% can be considered for a single carbon ion hit in the cell nucleus [21,22]. Therefore, unexpected hits of the cell nucleus may dominate the radiation effect and need to be excluded.

3.2. Targeted irradiation accuracy

Polycarbonate foil was irradiated with 5,120 ions in a matrix configuration of the size of 13.2 µm^2, as described in detail in Section 2.2. The polycarbonate foil serves as a solid state nuclear track detector

and can be used to visualize single ion hits by standard brightfield transmission light microscopy [23]. This irradiated target is referred to as target 1. In Fig. 3A, a microscopy image of target 1 is shown and in Fig. 3B the outline of the target area. A description of how the target areas were determined on the etched polycarbonate is given in Section 2.5. The center point of the target area was calculated by determining the center of mass. The maximum distance from the center point to the furthest edge of the target area is denoted as target radius. This radius is represented by the yellow circle in Fig. 3C and has a size of 6.5 µm. The maximum target radius of all targets irradiated for this study is 10 µm. This radius is shown in Fig. 3C by the red circle. Only ions farther than 10 µm from the target are included in the halo and considered in the evaluation.

Target 1 was irradiated with 55 MeV C^{5+} ions with object slit opening of 20 µm × 10 µm, divergence slit opening of 50 µm × 100 µm, and no aberration correction using supraloops. These were the same settings as for the targeted cell irradiation. Fig. 4A shows all ion hits of target 1 on the etched polycarbonate. The hits occur not only in the target area, marked by an arrow, but also outside. The quantification of parasitic halo hits is shown in Fig. 4G and H. In Fig. 4G, the ion hits of target 1 are depicted with red squares. The horizontal and vertical distributions of ion hits are shown with histograms above and on the right. A total of 218, i.e. 4.3% of the irradiated ions hit the polycarbonate outside the target area at distances of up to 600 µm from the center of the target. Almost all of these hits occurred in the lower right in an area of 150,000 µm^2. In Fig. 4H, the radial distances of halo ion hits are depicted. The mean radial distance of target 1, depicted by a black horizontal line, was 258 µm with a standard deviation of 96 µm, shown by an error bar.

3.3. Estimation of the dose induced by halo ions

The carbon ions had an LET of 365 keV/µm at the cell level. One carbon ion deposited a dose of 0.73 Gy in the cell nucleus. Therefore, the halo with an area of 150,000 µm^2 deposited a mean dose of $D_{halo} = 0.086$ Gy. In Fig. 5A, the halo area of one target is outlined in yellow in comparison to the cell's location in the fluorescence image of the irradiated cell population. The halo area is large enough to overlap almost all cells in the cell area consisting of 74 cells. The locations of the cells and the targets were recorded by the microscope at irradiation. The cell area was irradiated with 74 targets (one target per cell in the cell area) and each of the targets had a halo of this extent and shape. The 74 halos partly overlapped, as the cells were densely seeded in an area of 126,000 µm^2, which is smaller than the measured halo area. To estimate the dose to the cell growth area applied just by the halo, the overlaps of the halos were calculated from the locations of the targets and the dose distribution solely caused by the halos was calculated based on the overlaps. For each halo, a homogeneous dose distribution was considered for simplification. Fig. 5B shows a heat map of the calculated dose distribution overlaid by the locations of cells. Coming from the upper left, the lower left, or the upper right corner the dose increases steadily towards the lower right corner and is the highest there. The maximal dose was 6.3 Gy, whereas the mean dose and standard deviation over the whole cell area was (2 ± 2) Gy. As this heatmap depicts, 23% of the cells received a dose higher than 3 Gy caused solely by the halos and 57% of the cells received a dose between 1 Gy and 3 Gy. 20% of the cells received a dose below 1 Gy. Solely 0.07% of the cells received halo doses less than 0.1 Gy.

This means that 80% of the cells, including the radiation-sensitive nuclei, were irradiated with doses > 1 Gy. High-LET particle-induced doses of this magnitude lead to significant cell killing, as known from radiation effects on eukaryotic and especially HeLa cell nuclei [21,22,40]. Therefore, the halo dose to the cell nuclei can be considered as one of the main factors responsible for cell growth inhibition as measured here. The irradiation of the cytoplasm is magnitudes of orders less lethal than the irradiation of the nuclei [34]. The DNA damage
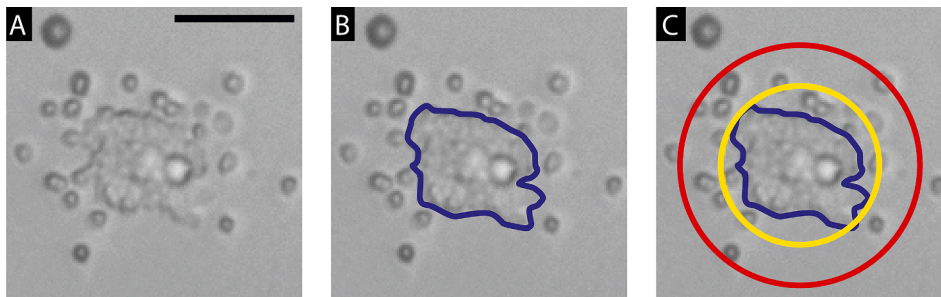
Fig. 3. Visualization of the evaluation of the target and the halo. In A, target 1 is shown. The scale bar in black has a size of 10 μm. In B, the outline of the target area is shown. The ion hits on the polycarbonate in the target area are so close together that they can no longer be distinguished. In C, a circle with the target radius of target 1 (6.5 μm) is depicted in yellow. The red circle in this image has the size of the maximum target radius in this study of 10 μm. For the halo, only ions farther from the target than the maximum target radius were considered. (For interpretation of the references to colour in this figure legend, the reader is referred to the web version of this article.)

induced by homogeneous irradiation of cells with doses > 1 Gy is so severe that it far outweighs the potential effects of mitochondrial depolarization. Therefore, the changed cell growth can be assumed to be a possible effect of the halo irradiation instead of the targeted irradiation of the mitochondria. In addition, oxidative stress caused by the high ROS production due to the high dose in the target area also may have influenced cell growth and should be tested in the future. However, in this publication we have focused in the following on the optimization of the microbeam and reduction of the halo, as a proper measurement of ROS would also require an accurate targeting of the irradiated ions. To avoid irradiation of the cell nuclei, the halo ions should not hit further than 5 μm from the target. As this distance to the cell nucleus can be well maintained as a buffer zone when irradiating the mitochondrial area. This estimation of parasitic dose shows, how important a proper quality assurance of the microbeam is when targeted irradiation effects in the cytoplasm are investigated. Subsequently, such beam analysis, as presented in this paper, should be performed to prevent inducing any bystander effects by halo irradiation.

3.4. Optimization of the halo by changing the ion sort to C^{6+}

The halo is most likely caused by charge changes or scattering events at the residual gas and slits in the beamline. The C^{5+} ions were used, as they are supplied with the highest yield by the accelerator [41]. These ions tend to lose their last electron during collisions in the beam path [42,43]. Ions with a different charge state are focused on a different focal spot by the superconducting multipoles and may be slightly deflected by parasitic magnetic dipoles in the beam line of the electrostatic scanning device, leading to a halo at the C^{5+} focal spot. Therefore, the probability of charge change events must be decreased to reduce the halo. The cross section for an electron capture of a 50 MeV C^{6+}-ion is 6 times smaller than the cross section for a 50 MeV C^{5+}-ion to lose an electron in nitrogen gas [43]. This difference is even higher when 55 MeV carbon ions traverse a carbon foil. Here, the electron capture cross section of a C^{6+}-ion is 19 times smaller than the electron loss cross section of a C^{5+}-ion. This value is derived from Shima et al. [41], the underlying derivation can be found in the supplementary. Overall, it can be concluded that the use of C^{6+} ions has the potential to reduce the halo significantly. Therefore, the halo formation for C^{6+} was experimentally tested. In Fig. 4, two C^{6+} targets (E and F) and their corresponding halos (B and C) are shown. As already visible by eye the halo size was significantly reduced. Target 4 is a single spot target irradiated with 10,000 ions using object slits of 20 μm × 10 μm and divergence slits of 50 μm × 100 μm just as for irradiation of target 1. Fig. 4G shows the ion distribution around the target, which is significantly reduced in target 4 compared to target 1. Furthermore the mean radial distance of ions in the halo was reduced by the use of C^{6+} (target 4) compared to C^{5+} (target 1) from (258 ± 96) μm to (16 ± 10) μm, shown in Fig. 4H. In target 4, only 3‰ of the ions were located in the halo with a maximum distance of 63 μm.

One has to note that the ion yield of the accelerator for C^{6+} was reduced by a factor of 10 compared to C^{5+} [41], resulting in a count rate of 300 Hz. At this low count rate, irradiation of the cells in a reasonable time is not possible. Therefore, it is necessary to work with larger slit openings while conserving the focal spot size. To achieve a count rate of 3 kHz for C^{6+} ions, it is necessary to work with object slits at 100 μm × 30 μm and divergence slit openings of 200 μm × 200 μm. To keep spot size small, the lens was equipped with correction wires, so-called supraloops. They were energized so that no aberrations were visible in the ray tracing pattern on the scintillator. In Fig. 4, Target 10 shows the optimized beam, with the optimized configuration as detailed evaluated in Section 3.5. Irradiation was performed using the 8 × 8 matrix and 5,120 ions and large slit openings. Fig. 4G and H show, that the distribution of halo ions was not as good as for target 4, but still much better than target 1. The mean radial distance was (31 ± 31) μm with a maximum distance of 168 μm. 8‰ of the ions (39 of 5,120 ions) were located in the halo. A reduction of MRD of 88% and a reduction of halo ions of 81% was achieved compared to the initial C^{5+} beam.

Based on target 10, another dose estimation was performed, which is shown in Fig. 5C. Target 10 causes a much smaller halo dose on the cell area than target 1. The halo area of target 10 is decreased to 4000 μm², which is about 3% of the halo area of target 1. Each halo area of target 10 deposits a mean dose of 0.57 Gy. The dose is accumulated closer to the cells than before optimization, but the halos of the individual cells overlap less frequently. Therefore, the dose estimation of target 10 results in a decreased mean dose and standard deviation of (1 ± 1) Gy with a maximum dose of 4.5 Gy. However, 11% of the cells were irradiated with >3 Gy and 73% with doses between 1 Gy and 3 Gy. Therefore, the optimization of the halo achieved in this study is still not enough to perform a proper targeted irradiation of non-cell nuclear targets with doses as high as 5 kGy.

To understand in detail which parameters affect the halo, a principle study on polycarbonate is presented in the next section.

3.5. Reduction of the halo by smaller beam spot sizes

In this study, different slit settings and the correction of lens errors by so-called supraloops were tested. For a better overview, the different slit settings were numbered due to their opening and are listed in Table 1.

First, the influences of slit settings and energizing supraloops on the beam spot size (BS) were investigated, as shown in Table 2. For this test, three polycarbonates were irradiated in the beamtimes of June 2018 (Polycarbonate foils 06/18) and September 2018 (Polycarbonate foils 09/18.2 and 09/18.3), as described in Section 2.4. In general, the BSs of September 2018 were worse than those of June 2018. In particular, the focus in y was not optimal. This was due to disturbing vibrations from noise in the experimental hall. Acoustic shielding was introduced to the head of the supporting structure of the lens, as described in Section 2.2. This allowed to reduce beam spot size again to a reasonable size, but not as small as before. The BSs for slit setting 1 were on all three polycarbonates better than for slit setting 4. In beamtime 06/18, the increase was 11% in x and 26% in y-direction. In beamtime 09/18, the increase in
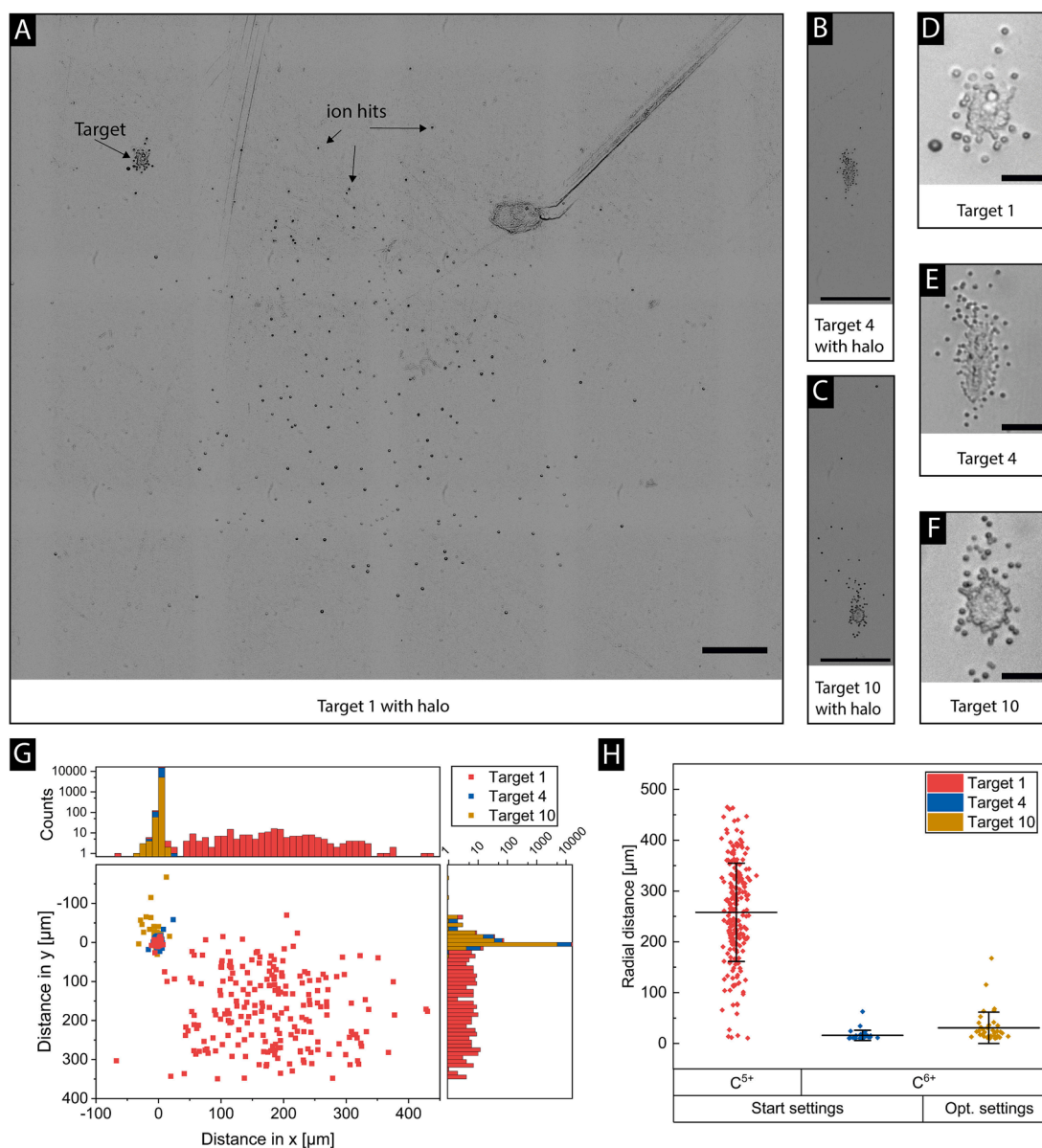
Fig. 4. Ion hits on polycarbonate and their evaluation. Target 1 was irradiated with the start settings, which were also used for the here described experiment. For target 4, the ion sort was changed to C^{6+} and 10,000 ions were irradiated. In target 10, the slits were adjusted to yield higher ion rates and with the help of supraloops lens errors were corrected. In A, B, and C all hits (target hits and hits in the halo) are depicted. Scale bar: 50 μm. In D, E, and F solely the targets are shown. Scale bar: 10 μm. For better visibility of the ion hits, the background of the microscopic images in A-F was reduced and the contrast was enhanced. In G, the ion distributions of the three targets are shown in one graph for a better comparison. Whereby, the center of the target area corresponds to the origin of the graph and the ion hits were drawn due to their respective Euclidian distances in x and y direction to the center of the target area. In the upper graph, a histogram of the hits in x direction is shown and on the right in y direction. The bar size is 10 μm, as this was chosen to be the minimum distance of halo ions due to overlaps of the etched ion hits close to the target. In H, the radial distances of the halo ions for the three targets are shown. The radial distances correspond to the Euclidian distance of the center of the ion hits to the center of the target area. Every rhomb depicts a halo ion. With black horizontal lines, the mean values are shown. The error bars are the standard deviations from the mean.

beam size was 70% in x and 13% in y-direction for polycarbonate 09/18.2 and 09/18.3. The BS is dependent on the object size given by the setting of the object slits and the divergence given by the settings of the divergence slits. Therefore, an increase in the beam spot size due to an increased opening of the object slits fits well to this dependency. For investigating the influence of energizing the supraloops, the BSs of September 2018 were compared, since in June 2018 a better focusing was achieved. Here, BS 3 and BS 4 were irradiated without supraloops and BS 5 and BS 6 with energizing supraloops. No difference within the uncertainty range could be found here between the beam spot sizes with and without supraloops, comparing BSs with slit setting 1 (BS 3 to BS 5) and BSs with slit setting 4 (BS 4 to BS 6). Therefore, no significant

differences could be found in the measured beam size, which came from energizing the supraloops. This result was contra intuitive to what was proposed in the design study of SNAKE [28]. The supraloops were installed to correct lens errors. Therefore, especially for the more open slit configuration 4, a difference was expected but could not be confirmed.

It was further investigated, whether the beam spot size influences the halo by irradiating 9 different targets (target 2–target 10) shown in Table 3. In Fig. 6A, the FWHM (full width at half maximum) of beam spot sizes in x and y-direction of all irradiated targets are shown. The error bars show the variation in beam spot size (standard deviation). The beam spot sizes marked with a star were measured with slit setting 1
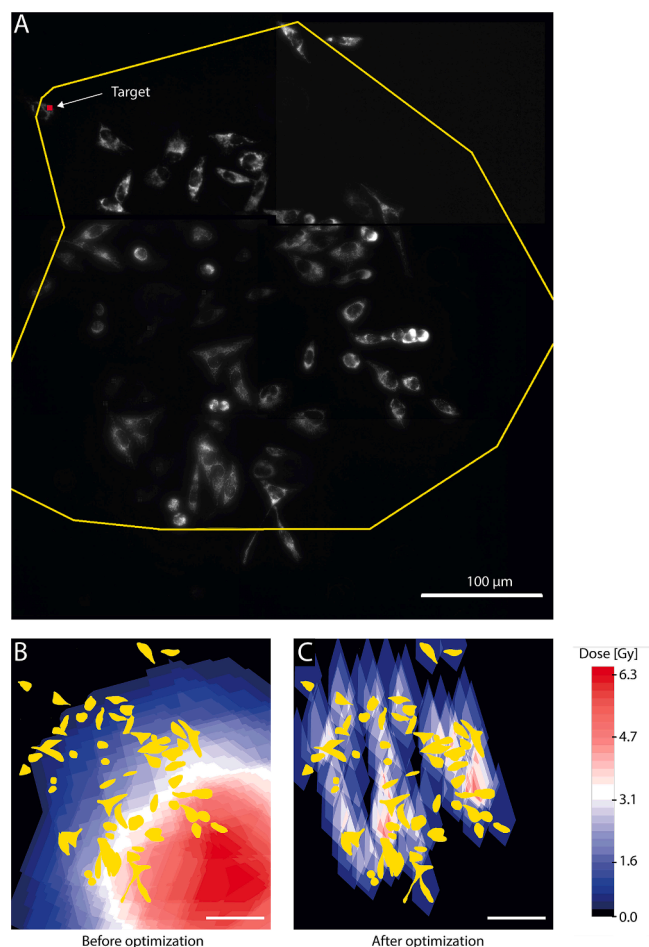
Fig. 5. Estimation of dose caused solely by the halo of targeted irradiation on the cells. In A, a fluorescent image of the cell area is shown, where the mitochondria are stained. In yellow the outline of a single halo area is indicated as induced by the target labeled with a red dot. In B and C heatmaps of the dose distribution caused by the halos of the irradiated targets are shown before optimization of the beam (B) and after optimization (C). In yellow the locations of the cells are indicated. (For interpretation of the references to colour in this figure legend, the reader is referred to the web version of this article.)

Table 1
The different slit settings tested in this study.

Slit setting number	Object slits		Divergence slits	
	Opening in x [µm]	Opening in y [µm]	Opening in x [µm]	Opening in y [µm]
1	20	10	50	100
2	20	20	100	100
3	100	50	50	100
4	100	30	200	200

instead of the slit settings 2 or 3 of the targets. In practice, it was observed that these three settings cause no difference in the beam spot size. Therefore, the beam spot size was only measured for setting 1. As Fig. 6A shows, target 1 to target 7 have the same beam spot sizes in x and y-direction. The beam spot size of target 8 is 37% larger in x and 23% in y. For targets 9 and 10, a 43% increase in x and a 38% increase in y was measured compared to target 1 to target 7. Overall, the targets irradiated in beam time 03/18 and 06/18 have smaller beam spot sizes than the targets of beam time 09/18.

Fig. 6B shows the MRDs (mean ± standard deviation) of each target as bars and the number of halo ions in the line plot. Target 1 and target 10 were irradiated with 5,120 ions in matrix configuration as used for

Table 2
Beam spot sizes (BS) measured for slit setting 1 and 4 and with and without supraloops. The polycarbonate ID indicates the month/year of beam time and the polycarbonate foil number.

ID	Slit setting	Supraloops	Polycarbonate ID	Beam spot size in x [µm]	Beam spot size in y [µm]
BS 1	1	Yes	06/18.3	1.14 ± 0.06	1.36 ± 0.06
BS 2	4	Yes	06/18.3	1.26 ± 0.06	1.71 ± 0.08
BS 3	1	No	09/18.2	1.15 ± 0.09	1.84 ± 0.09
BS 4	4	No	09/18.2	1.99 ± 0.14	2.08 ± 0.10
BS 5	1	Yes	09/18.3	1.33 ± 0.07	1.97 ± 0.14
BS 6	4	Yes	09/18.3	2.23 ± 0.18	2.21 ± 0.23

the targeted irradiation of cells. Target 2 to target 9 were irradiated with 10,000 ions in one spot for better comparability with the beam spot sizes. Here, it can be seen, that target 2 to target 10 have significantly smaller MRDs than target 1, resulting from the change of charge state, as described in section 3.4. No correlation between slit setting and MRD can be found. For example, the same MRDs are measured for target 3 and target 4. Target 3 was irradiated with the more open slit setting 3, and target 4 with the most closed slit setting 1. On the other hand, target 5 was irradiated with the same slit setting as target 4 and has a 36% higher MRD. In contrast, the number of halo ions tends to anticorrelate with the opening of the slits. Target 3, target 6, and target 7 were irradiated with the more open slit settings 3 and 4 and have approx. 40% fewer ions in their halo than target 2, target 4, and target 5, which were irradiated with the more closed slit settings 1 and 2. As no significant impact of the slit settings was observed on the halo and slit setting 4 yields the highest ion count rate, all targets were irradiated with this slit setting in beamtime 09/18. Now it was investigated, whether the supraloops affect the halo. Therefore, target 8 was irradiated without supraloops and target 9 with supraloops. The supraloops do not affect the MRD, which was expected as there was also no effect on the beam size. However, the fraction of halo ions could further be reduced from 6‰ to 5‰.

It can be concluded that the use of C^{6+} instead of C^{5+}-ions reduced the size of the halo and the number of ions in the halo. The slit opening needed to be increased from 20 µm × 10 µm to 100 µm × 30 µm for the object slits and from 50 µm × 100 µm to 200 µm × 200 µm for divergence slits, to preserve the count rate, due to the low yield of C^{6+} ions from the tandem accelerator. This can be done as the increased beam spot size does not affect the halo of the irradiated target. Furthermore, larger slit openings and energizing of supraloops result in a decreased number of halo ions. Therefore, the optimized beam setting for targeted irradiation of mitochondria, which was achievable in the SNAKE setup, was considered to be C^{6+} ions with energized supraloops at slit settings of 100 µm × 30 µm, 200 µm × 200 µm. The optimized irradiation was performed in target 10, which was again an 8 × 8 matrix irradiation with 5,120 ions. A reduction of MRD of 88% and a reduction of halo ions of 81% was achieved compared to the initial C^{5+} beam. The dose estimation for this optimized target is discussed in Section 3.4.

The microscopy images of the here discussed targets can be found in Supplementary Figs. 1–10. The repetitive pattern of dark spots on these images occurred due to dust in the optical light path of the used microscope, but did not have any influence on the evaluation of the images, as they could be easily distinguished from the ion hits. In Supplementary Figs. 2–7, the target areas are broader, due to a higher beam spot size in y-direction than in x-direction. The two dark spots in target 5 to target 7 (Supplementary Figs. 5–7) originate from the etching process and not from an increased ion density at these spots. Solid state nuclear track detectors like polycarbonate are very good in detecting single ions. However, if the ion densities are too high that the etched hits are overlapping each other and can no longer be distinguished, no conclusion can be drawn about the ion densities. Here other factors, like the level of etching, inhomogeneities in the material or the energy

Table 3

The settings, beam time, in which the targets were irradiated, the beam spot sizes and the results of halo measurements for all targets are listed here. The slit settings are given in the following order: object slit x × object slit y, divergence slit x × divergence slit y. The beam spot size is given this way: x-direction, y-direction. Target 1 was irradiated in beamtime 03/18, targets 2 – 7 in beamtime 06/18, and targets 9 and 10 in 09/18.

| Target	Number of ions	Ion sort	Slit setting number	Slit openings [μm]	Beam spot [μm]	MRD [μm]	Standard deviation [μm]	Maximum distance [μm]	Number of halo ions
1	5,120	C^{5+}	1	20 × 10, 50 × 100	1.45 ± 0.06 1.60 ± 0.08	258	96	465	218
2	10,000	C^{6+}	2	20 × 20, 100 × 100	1.14 ± 0.06 1.36 ± 0.06	32	22	93	34
3	10,000	C^{6+}	3	100 × 50, 50 × 100	1.14 ± 0.06 1.36 ± 0.06	15	7	33	12
4	10,000	C^{6+}	1	20 × 10, 50 × 100	1.14 ± 0.06 1.36 ± 0.06	16	10	63	31
5	10,000	C^{6+}	1	20 × 10, 50 × 100	1.14 ± 0.06 1.36 ± 0.06	25	19	83	37
6	10,000	C^{6+}	3	100 × 50, 50 × 100	1.14 ± 0.06 1.36 ± 0.06	19	8	39	23
7	10,000	C^{6+}	4	100 × 30, 200 × 200	1.26 ± 0.06 1.71 ± 0.08	20	12	46	26
8	10,000	C^{6+}	4	100 × 30, 200 × 200	1.99 ± 0.14 2.08 ± 0.10	33	37	202	60
9	10,000	C^{6+}	4	100 × 30, 200 × 200	2.23 ± 0.18 2.21 ± 0.23	32	47	232	49
10	5,120	C^{6+}	4	100 × 30, 200 × 200	2.23 ± 0.18 2.21 ± 0.23	31	31	168	39
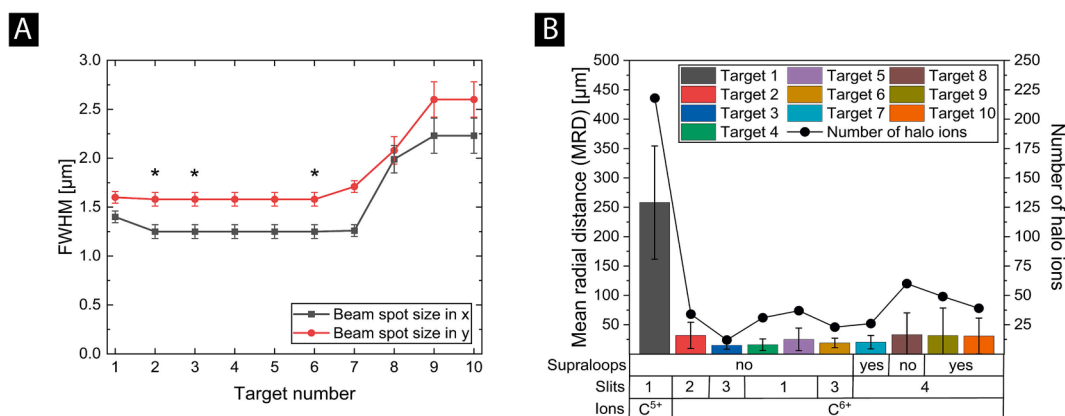
Fig. 6. Evaluation of the halo of targets irradiated with different settings and their corresponding beam spot sizes. In A, the beam spot sizes for every target in x and y-direction are depicted by dots connected with lines. The beam spot sizes were derived from the FWHMs of Gaussian fits, as more detailed explained in Section 2.4. The error bars show an uncertainty of 0.9 μm. This uncertainty originates from the measuring method. Beam spot sizes marked by a star were measured with the slit setting 1 instead of the actual slit settings of the targets. In B, the bars show the MRDs (mean radial distances of the halo ions), which were further away from the target than 10 μm. The errors denote the standard deviations. The number of halo ions is shown by black dots connected with lines and has its own y-axis on the right. The line, which connects the dots is included to increase the visibility of the number of ions in contrast to the MRDs shown by bars and has no further scientific meaning. Below the graph, a table of the different settings is shown.

deposition are more relevant. Comparing target 2–4 with targets 5–7 makes clear, that these dark spots originate from a higher etching level.

The here presented results show, that the change of ion type led to a significant reduction of the halo. The slit settings and supraloops had minor effects on the number of halo ions. Furthermore, we observed that outer influences like acoustic noise or vibrations play an important role. For example, it could be seen that target 2 to target 7 had all smaller MRDs, smaller numbers of halo ions, and smaller beam spot sizes than target 9 to target 10, which were irradiated in the following beam time. Microbeams such as SNAKE are very sensitive to outer influences. The ion beam is focused on a distance of 30 m. So, small acoustic and mechanical noises, for example of vacuum pumps, can lead to a spread of the ion beam. As SNAKE consists of a three-meter high cryotank hosting the superconducting lenses, the setup is prone to uptake vibrations from the surrounding. Turning off all devices which cause these vibrations and noises is only possible to a limited extent. Most of these devices are indispensable in the working environment of an accelerator like vacuum

pumps and cooling systems. Therefore, this has to be kept in mind for a new design of a microbeam. To understand how the halo emerges, a closer look on the beamline is necessary. Here, different interactions are possible. The ions can scatter, capture an electron, or lose one. These interactions can happen at residual vacuum molecules, in the transparency zone of the slits, or in the walls of the beam line. As discussed in Section 3.4, the probability of a charge exchange could be widely reduced by choosing C^{6+}-ions. However, this reduction cannot be explained by the residual vacuum of the beamline alone. The vacuum in the beamline has a pressure of 10^{-7} mbar, consisting mainly of light ions like H_2 and maybe N_2 molecules. The cross section for an electron loss of a 31.8 MeV C^{5+} ion is $\sigma_{56} = 0.66$ cm^2/μg [44]. It can be estimated, that the 30 m SNAKE beamline contains $7.5 \ 10^{-10}$ g/cm^2, assuming only residual nitrogen molecules in the vacuum. Therefore, a probability of such a charge changing event can be calculated by multiplying these two values and leads to a probability of 0.04%. This is only a rough estimation of the probability, but it shows that by the vacuum alone a halo

consisting of 4% of halo ions cannot be explained. Hence, charge changes must also happen in the transparency zone of the slits or in the walls of the beam line. Since both, the walls and the slits, are made of heavier atoms, high-angle scattering can also be caused. This effect cannot be reduced by changing the ion charge state. This is the reason, why also the optimized targets have a halo.

4. Conclusion

In this study, an experimental set-up for targeted irradiation of mitochondria in human cells followed by long-term live-cell imaging is presented and a first successful experiment was conducted. The performed experiment shows, that already low numbers of ions, hitting targets outside of the focus of an ion microbeam can have a significant impact on experimental outcomes in biological experiments. The results of this experiment showed the importance of a proper beam spot analysis, as the irradiated ions hit not only in the target but also up to 500 μm outside and formed a halo. Especially, high-LET ions, which deposit a large amount of dose in one ion traversal can increase the unwanted effect caused by an ion halo.

Methods for measuring the halo and the beam spot size were presented here. With these methods, the effects of different settings (charge state, slit opening, and lens error correction) of the microbeam and the role of the beam spot size on the halo were tested. A significant reduction of 97% of the halo area could be achieved by changing the ions' charge state to C^{6+}. Whereas, the slit opening, the lens error correction with supraloops, and the beam spot size did not influence the mean radial distances of halo ions, but had minor influences on the number of halo ions. Therefore, it was chosen to use C^{6+} ions, the most open slit setting 4, and to energize the supraloops as an optimized configuration. However, the optimized beam still formed a halo around the target. Although the optimized halo is smaller than the initial one. It still induces a mean parasitic dose of (1 ± 1) Gy over the whole cell area. This dose is still too high if it interacts with cell nuclei. Therefore, further investigations on the formation of the halo and subsequent improvements are necessary to investigate the effects of depolarizing mitochondria on overall cell survival.

CRediT authorship contribution statement

Sarah Rudigkeit: Conceptualization, Methodology, Validation, Formal analysis, Investigation, Writing – original draft. **Nicole Matejka:** Investigation, Writing – review & editing. **Matthias Sammer:** Investigation, Writing – review & editing. **Dietrich W.M. Walsh:** Conceptualization, Methodology, Investigation, Writing – review & editing. **Günther Dollinger:** Conceptualization, Methodology, Resources, Funding acquisition, Writing – review & editing. **Judith Reindl:** Conceptualization, Methodology, Validation, Formal analysis, Investigation, Writing – original draft, Supervision.

Declaration of Competing Interest

The authors declare that they have no known competing financial interests or personal relationships that could have appeared to influence the work reported in this paper.

Appendix A. Supplementary material

Supplementary material to this article can be found online at https://doi.org/10.1016/j.nimb.2023.07.004.

References

[1] D.W.M. Walsh, C. Siebenwirth, C. Greubel, K. Ilicic, J. Reindl, S. Girst, G. Muggiolu, M. Simon, P. Barberet, H. Seznec, H. Zischka, G. Multhoff, T.E. Schmid, G. Dollinger, Live cell imaging of mitochondria following targeted irradiation in situ reveals rapid and highly localized loss of membrane potential, Sci. Rep. 7 (2017) 46684, https://doi.org/10.1038/srep46684.

[2] A. Buchfellner, L. Yurlova, S. Nüske, A.M. Scholz, J. Bogner, B. Ruf, K. Zolghadr, S. E. Drexler, G.A. Drexler, S. Girst, C. Greubel, J. Reindl, C. Siebenwirth, T. Romer, A. A. Friedl, U. Rothbauer, A new nanobody-based biosensor to study endogenous PARP1 in vitro and in live human cells, PLoS One 11 (2016), e0151041, https://doi.org/10.1371/journal.pone.0151041.

[3] C. Siebenwirth, C. Greubel, G.A. Drexler, J. Reindl, D.W.M. Walsh, B. Schwarz, M. Sammer, I. Baur, H. Pospiech, T.E. Schmid, G. Dollinger, A.A. Friedl, Local inhibition of rRNA transcription without nucleolar segregation after targeted ion irradiation of the nucleolus, J. Cell Sci. 132 (2019), https://doi.org/10.1242/jcs.232181.

[4] R.E. Zirkle, W. Bloom, Irradiation of parts of individual cells, Science 117 (1953) 487–493, https://doi.org/10.1126/science.117.3045.487.

[5] M. Suzuki, N. Usami, Cell-killing effect by the targeted cytoplasmic irradiation in normal human fibroblasts with monochromatic X-ray microbeams (2), Photon Fact. Act. Rep. 2016 (2017).

[6] T.R. Munro, The relative radiosensitivity of the nucleus and cytoplasm of chinese hamster fibroblasts, Radiat. Res. 42 (1970) 451, https://doi.org/10.2307/3572962.

[7] H. Zhou, G. Randers-Pehrson, C.A. Waldren, D. Vannais, E.J. Hall, T.K. Hei, Induction of a bystander mutagenic effect of alpha particles in mammalian cells, Proc. Natl. Acad. Sci. U. S. A. 97 (2000) 2099–2104, https://doi.org/10.1073/pnas.030420797.

[8] G. Schettino, M. Folkard, K.M. Prise, B. Vojnovic, K.D. Held, B.D. Michael, Low-dose studies of bystander cell killing with targeted soft X rays, Radiat. Res. 160 (2003) 505–511, https://doi.org/10.1667/rr3060.

[9] C. Shao, Y. Furusawa, M. Aoki, K. Ando, Role of gap junctional intercellular communication in radiation-induced bystander effects in human fibroblasts, Radiat. Res. 160 (2003) 318–323, https://doi.org/10.1667/rr3044.

[10] K.M. Prise, O.V. Belyakov, M. Folkard, B.D. Michael, Studies of bystander effects in human fibroblasts using a charged particle microbeam, Int. J. Radiat. Biol. 74 (1998) 793–798, https://doi.org/10.1080/095530098141087.

[11] M. Durante, A.A. Friedl, New challenges in radiobiology research with microbeams, Radiat. Environ. Biophys. 50 (2011) 335–338, https://doi.org/10.1007/s00411-011-0373-x.

[12] V. Hable, G.A. Drexler, T. Brüning, C. Burgdorf, C. Greubel, A. Derer, J. Seel, H. Strickfaden, T. Cremer, A.A. Friedl, G. Dollinger, Recruitment kinetics of DNA repair proteins Mdc1 and Rad52 but not 53BP1 depend on damage complexity, PLoS One 7 (2012), e41943, https://doi.org/10.1371/journal.pone.0041943.

[13] C. Penterling, G.A. Drexler, C. Böhland, R. Stamp, C. Wilke, H. Braselmann, R. B. Caldwell, J. Reindl, S. Girst, C. Greubel, C. Siebenwirth, W.Y. Mansour, K. Borgmann, G. Dollinger, K. Unger, A.A. Friedl, Depletion of Histone Demethylase Jarid1A Resulting in Histone Hyperacetylation and Radiation Sensitivity Does Not Affect DNA Double-Strand Break Repair, PLoS One 11 (2016), e0156599, https://doi.org/10.1371/journal.pone.0156599.

[14] P.S. Amenta, The effects of ultraviolet microbeam irradiation on the eosinophil granular leukocytes of Triturus viridescens, Anat. Rec. 142 (1962) 81–87, https://doi.org/10.1002/ar.1091420112.

[15] P.P. Dendy, C.L. Smith, Effects on DNA synthesis of localized irradiation of cells in tissue culture by (i) a u.v. microbeam and (ii) an α-particle microbeam, Proc. R. Soc. Lond., B, Biol. Sci. 160 (1964) 328–344.

[16] A.M. Kuzin, A.A. Wainson, Effect of alpha-particle microbeam irradiation on the synthesis of deoxyribonucleic acid in tissue culture, Nature 212 (1966) 819–820.

[17] S. Takeda, S. Naruse, R. Yatani, Effects of ultra-violet microbeam irradiation of various sites of HeLa cells on the synthesis of RNA, DNA and protein, Nature 213 (1967) 696–697.

[18] W.W.-Y. Kam, R.B. Banati, Effects of ionizing radiation on mitochondria, Free Radic. Biol. Med. 65 (2013) 607–619, https://doi.org/10.1016/j.freeradbiomed.2013.07.024.

[19] P.E. Porporato, N. Filigheddu, J.-S. Pedro, G. Kroemer, L. Galluzzi, Mitochondrial metabolism and cancer, Cell Res. 28 (3) (2018) 265–280.

[20] C. Wang, R.J. Youle, The role of mitochondria in apoptosis*, Annu. Rev. Genet. 43 (2009) 95–118, https://doi.org/10.1146/annurev-genet-102108-134850.

[21] T. Friedrich, K. Ilicic, C. Greubel, S. Girst, J. Reindl, M. Sammer, B. Schwarz, C. Siebenwirth, D.W.M. Walsh, T.E. Schmid, M. Scholz, G. Dollinger, DNA damage

interactions on both nanometer and micrometer scale determine overall cellular damage, Sci. Rep. 8 (2018) 16063, https://doi.org/10.1038/s41598-018-34323-9.

[22] J.S. Bedford, E.J. Hall, Survival of HeLa Cells Cultured in In-vitro and Exposed to protracted Gamma-Irradiation, Int. J. Radiat. Biol. Relat. Stud. Phys. Chem. Med. 7 (1963) 377–383, https://doi.org/10.1080/09553006314551311.

[23] C. Hepburn, A.H. Windle, Solid state nuclear track detectors, J. Mater. Sci. 15 (1980) 279–301, https://doi.org/10.1007/PL00020061.

[24] K.-D. Greif, H.J. Brede, D. Frankenberg, U. Giesen, The PTB single ion microbeam for irradiation of living cells, Nucl. Instrum. Methods Phys. Res. Sect. B: Beam Interact. Mater. Atoms 217 (2004) 505–512, https://doi.org/10.1016/j.nimb.2003.11.082.

[25] T. Ikeda, M. Ikekame, Y. Hikima, M. Mori, S. Kawamura, T. Minowa, W.-G. Jin, Profile measurements of MeV ion microbeams in atmosphere extracted from single tapered glass capillaries with an end window, Nucl. Instrum. Methods Phys. Res. Sect. B: Beam Interact. Mater. Atoms 470 (2020) 42–47, https://doi.org/10.1016/j.nimb.2020.03.004.

[26] T. Vallentin, M. Moser, S. Eschbaumer, C. Greubel, T. Haase, P. Reichart, T. Rösch, G. Dollinger, A microbeam slit system for high beam currents, Nucl. Instrum. Methods Phys. Res. Sect. B: Beam Interact. Mater. Atoms 348 (2015) 43–47, https://doi.org/10.1016/j.nimb.2014.12.015.

[27] G. Datzmann, G. Dollinger, C. Goeden, A. Hauptner, H.-J. Körner, P. Reichart, O. Schmelmer, The Munich microprobe SNAKE: First results using 20 MeV protons and 90 MeV sulfur ions, Nucl. Instrum. Methods Phys. Res. Sect. B: Beam Interact. Mater. Atoms 181 (2001) 20–26, https://doi.org/10.1016/S0168-583X(01)00549-3.

[28] G. Datzmann, Aufbau und Charakterisierung des Hochenergie Rasterionenmikroskops SNAKE. Dissertation, München, 2002.

[29] C. Siebenwirth, Gezielte Bestrahlung zellulärer und nukleärer Substrukturen am Ionenmikrostrahl SNAKE. Dissertation, Neubiberg, 2017.

[30] V. Hable, C. Greubel, A. Bergmaier, P. Reichart, A. Hauptner, R. Krücken, H. Strickfaden, S. Dietzel, T. Cremer, G.A. Drexler, A.A. Friedl, G. Dollinger, The live cell irradiation and observation setup at SNAKE, Nucl. Instrum. Methods Phys. Res. Sect. B: Beam Interact. Mater. Atoms 267 (2009) 2090–2097, https://doi.org/10.1016/j.nimb.2009.03.071.

[31] J. Schindelin, I. Arganda-Carreras, E. Frise, V. Kaynig, M. Longair, T. Pietzsch, S. Preibisch, C. Rueden, S. Saalfeld, B. Schmid, J.-Y. Tinevez, D.J. White, V. Hartenstein, K. Eliceiri, P. Tomancak, A. Cardona, Fiji: an open-source platform for biological-image analysis, Nat. Methods 9 (2012) 676–682, https://doi.org/10.1038/nmeth.2019.

[32] S. Preibisch, S. Saalfeld, P. Tomancak, Globally optimal stitching of tiled 3D microscopic image acquisitions, Bioinformatics 25 (2009) 1463–1465, https://doi.org/10.1093/bioinformatics/btp184.

[33] H.T. Epstein, Identification of radiosensitive volume with nucleic acid volume, Nature 171 (1953) 394–395, https://doi.org/10.1038/171394a0.

[34] H. Zhou, M. Hong, Y. Chai, T.K. Hei, Consequences of cytoplasmic irradiation: studies from microbeam, J. Radiat. Res. 50 (Suppl.A) (2009) A59–A65.

[35] I. Szumiel, Ionizing radiation-induced oxidative stress, epigenetic changes and genomic instability: the pivotal role of mitochondria, Int. J. Radiat. Biol. 91 (2015) 1–12, https://doi.org/10.3109/09553002.2014.934929.

[36] P.A. Riley, Free radicals in biology: oxidative stress and the effects of ionizing radiation, Int. J. Radiat. Biol. 65 (1994) 27–33, https://doi.org/10.1080/09553009414550041.

[37] Z. Zou, H. Chang, H. Li, S. Wang, Induction of reactive oxygen species: an emerging approach for cancer therapy, Apoptosis 22 (2017) 1321–1335, https://doi.org/10.1007/s10495-017-1424-9.

[38] L.J. Wu, G. Randers-Pehrson, A. Xu, C.A. Waldren, C.R. Geard, Z. Yu, T.K. Hei, Targeted cytoplasmic irradiation with alpha particles induces mutations in mammalian cells, Proc. Natl. Acad. Sci. U. S. A. 96 (1999) 4959–4964, https://doi.org/10.1073/pnas.96.9.4959.

[39] T.K. Hei, L.J. Wu, S.X. Liu, D. Vannais, C.A. Waldren, G. Randers-Pehrson, Mutagenic effects of a single and an exact number of alpha particles in mammalian cells, Proc. Natl. Acad. Sci. U. S. A. 94 (1997) 3765–3770, https://doi.org/10.1073/pnas.94.8.3765.

[40] R.A. Deering, R. Rice Jr, Heavy Ion Irradiation of HeLa Cells on JSTOR, Radiat. Res. 17 (1962) 774–786.

[41] K. Shima, N. Kuno, M. Yamanouchi, H. Tawara, Equilibrium charge fractions of ions of Z = 4–92 emerging from a carbon foil, Atomic Data Nucl. Data Tables 51 (2) (1992) 173–241.

[42] H. Knudsen, L.H. Andersen, H.K. Haugen, P. Hvelplund, Electron Loss from Fast One-Electron Ions Colliding With He, N_2, and Ar, Physica Scripta 26 (1982) 132–140, https://doi.org/10.1088/0031-8949/26/3/002.

[43] T. Tonuma, Y. Miyaz, T. Karasawa, I. Kohno, Charge Exchange of Carbon and Nitrogen Ions in Nitrogen Gas, Jpn. J. Appl. Phys. 9 (1970) 1306–1311, https://doi.org/10.1143/JJAP.9.1306.

[44] G. Dollinger, M. Boulouednine, A. Bergmaier, T. Faestermann, Nonequilibrium charge states of recoil ions in high resolution elastic recoil detection analysis, Nucl. Instrum. Methods Phys. Res. Sect. B: Beam Interact. Mater. Atoms 136–138 (1998) 574–578, https://doi.org/10.1016/S0168-583X(97)00662-9.